# Chapter-6

## $SrFeO_{3-\delta}$: A Novel $Fe^{4+} \leftrightarrow Fe^{2+}$ Redox Mediated Pseudocapacitive Electrode in Aqueous Electrolyte

# Chapter-6

## $SrFeO_{3-\delta}$: A Novel $Fe^{4+} \leftrightarrow Fe^{2+}$ Redox Mediated Pseudocapacitive Electrode in Aqueous Electrolyte

### 6.1 Introduction

$RuO_2$ was the first and most extensively studied capacitance material to show pseudo-capacitance behavior. It continues to be an excellent capacitance material due to its high chemical stability and conductivity. [1, 2] However, its commercial application is limited due to high cost and scarcity of the material. $MnO_2$ was first reported to possess pseudocapacitive behavior in 1999 by Lee and Goodenough. [3] Due to its low cost, abundance and high 'theoretical' capacity was extensively studied as a replacement of $RuO_2$. [2, 4-7] Investigation of other lower-cost alternatives such as NiO, $V_2O_5$, spinels-$Co_3O_4$, $Fe_3O_4$, mixed spinel-$NiCo_2O_4$, layered hydroxides-$Ni(OH)_2$, $Co(OH)_2$ are being vigorously pursued. However, their inherent poor electrical and ionic conductivity limit their practical applications. [8-18] Therefore, research on combining these transition-metal containing ECs with conductive carbon and/or increasing their surface area by nanostructure engineering is very much in vogue to access the full theoretical capacitance of these materials and to enhance the electrical conductivity. [19-23]

Despite the hefty research effort on the development of a high-energy, high-power ECs, an important class of oxides, perovskite-type $ABO_3$, has received little attention. The perovskite-structure is robust and it can accommodate a wide range of electronic properties by doping on either or both the A-site and B- site positions and by varying the oxygen content. [24-28] Perovskite materials have recently received much interest as active components in various electronic devices, such as sensors, light-

emitting diodes, and solar cells. They belong to promising materials that could be used in low-cost, high-performance electronic applications. Wilde *et al*. reported that un-doped and doped $SrRuO_3$ exhibited a capacitance of ~10-30 $Fg^{-1}$; Wohlfahrt-Mehrens *et al*. increased its capacitance to 270 F $g^{-1}$ by modifying the $SrRuO_3$ synthesis conditions. [24-26] Hwang *et al*. and Mefford *et al*. recently reported a specific capacitance of ~160 and ~610 F $g^{-1}$ for MnO-coated $LaNiO_3$ and $LaMnO_3$ respectively, [27, 28] that was followed by Cao *et al*. who reported a capacitance of ~750 F $g^{-1}$ for Sr doped $LaCoO_3$.[29] Recently, charge storage mechanism of oxygen-anion intercalation was proposed and perovskites received a lot of attention as an anode material for supercapacitors. Hao-shan Nan *et al*. reviewed recent advances in perovskite oxides for anion-intercalation supercapacitor. [30] Carbonaceous materials (include activated carbons (AC), carbon nanotubes (CNTs), and graphene) are often utilized electrode materials for energy storage devices. They are appropriate for EDLCs Supercapacitor and used as negative electrode because of their high surface area, easily accessible materials, porous structural morphology, and superior electrical conductivity. [31]

I made the extensive analysis of perovskite $SrFeO_{3-\delta}$ (prepared by flux-method) electrochemical performance, structural characteristics, stability, and compatibility with electrolytes and investigated it as a negative electrode material for electrochemical applications. The ultimate objective is to develop a better understanding to its capabilities and limitations for energy storage and conversion applications.

In this chapter, we present the detailed study of perovskite-type $SrFeO_{3-\delta}$ showing superior pseudo-capacitive charge storage as a negative electrode of pseudo-capacitor or supercapacitor with superior stability. In stoichiometric $SrFeO_3$, the Fe should ideally be in the +4 oxidation state but in actuality Fe assumes a mixed oxidation state

of +4 and +3 owing to a variable oxygen content that provides a mixed-valent iron with a higher metallicity of $SrFeO_{3-\delta}$ than $SrRuO_3$; so-called *'bad metal'* where Ru exist in only the +4 oxidation state.[26] We obtained capacitance of 743 F $g^{-1}$ at a scan rate of 1 A $g^{-1}$ for $SrFeO_{3-\delta}$: acetylene-black: polyvinylidene difluoride (PVDF) (7:2:1 by weight) composite electrode with a capacity retention of more than 93% over 2500 repeated cycles. Results show that $SrFeO_{3-\delta}$ offers a cheap and abundant alternative to expensive and scarce $RuO_2$ which is a state-of-the-art pseudocapacitive material. Good cycle-life and high capacitance value of the perovskite $SrFeO_{3-\delta}$ electrodes are attributed to its good electrical conductivity and robust crystal structure.

## 6.2 Experimental:

### 6.2.1 Synthesis Method

All the chemicals were obtained from Alfa-Aesar and used without any further purification. For the synthesis of $SrFeO_{3-\delta}$, a stoichiometric amount of $SrCl_2$ (99.5+% metals basis) and $Fe_2O_3$ (99+% metals basis) were first mixed in an agate mortar pestle followed by mixing in KOH pellets (85% pellets; acts as a fluxing agent) in molar ratio 2:1:10. Subsequently, the grounded mixture was transferred to an alumina crucible and heated at 400° C overnight in a box furnace. The next day, the reaction mixture was allowed to cool down to room temperature and washed thoroughly several times with de-ionized water and ethanol to remove the flux residues. The resulting product was dried, ground and sintered at 800°C for 12 h.

## 6.3 Results and Discussions:

### 6.3.1 XRD Studies

The XRD pattern of the powder obtained after washing out the KOH flux was amorphous in nature; after sintering at 800 °C, the powder was identified as a single-phase perovskite material. Rietveld refinement of the powder XRD pattern of strontium

ferrate oxide, represented by nominal formula $SrFeO_{3-\delta}$, prepared by flux-method was carried out by simultaneously varying the structure factor, background, unit-cell profile, and isotropic thermal parameters; all the peaks in the diffraction pattern, Fig. 6.1a, were indexed the standard JCPDS card no. 40-0905 with respect to the cubic P m-3m (space group no. 221) and the unit-cell parameter [$a$ = 3.8603(2) Å] was in close agreement with that given in the literature [32-34] showing that the phase has formed with no detectable impurities; the compound was shining black in color. VESTA image (Fig. 6.1b**)** shows $SrFeO_{3-\delta}$ adopt a cubic-perovskite structure where due to oxygen vacancy part of Fe remain in +3 oxidation state to maintain charge neutrality (see Fig. 6.2a); however, bulk ceramic samples acquire a wide range of oxygen non-stoichiometry with a mixed oxidation state of iron exhibiting metallic conductivity. [32, 34, 35]

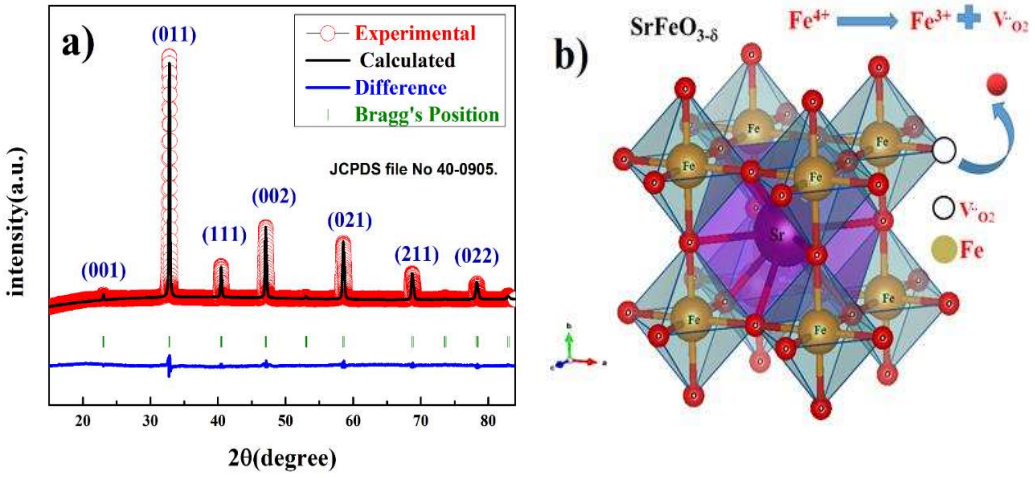


**Figure 6.1 (a)** Rietveld refined powder-XRD pattern

and **(b)** Vesta image of $SrFeO_{3-\delta}$.

Consequently, the oxygen content of our sample of $SrFeO_{3-\delta}$ was determined by iodometric titrations and found to be 2.96 ± 0.01, suggesting that ~92% of Fe is in +4 oxidation state and, therefore, our strontium ferrite oxide prepared by flux method can be expressed as $SrFe^{4+}_{0.92}\ Fe^{3+}_{0.08}\ O_{2.96}$.

### 6.3.2 XPS Analysis

The chemical state of iron was also investigated using XPS. The core-level binding-energy spectra of Fe 2*p*, Fig. 6.1c, for the as-synthesized $SrFeO_{3-\delta}$ could be fitted with two pairs of doublet. The pair that appears at higher binding energy is assigned to $Fe^{4+}$; the lower energy pair belongs to $Fe^{3+}$; the $2p_{3/2}$ and $2p_{1/2}$ peak positions are summarized in Table 6.1. The presence of a weak satellite indicates that the majority of the iron is in +4 oxidation state [33]

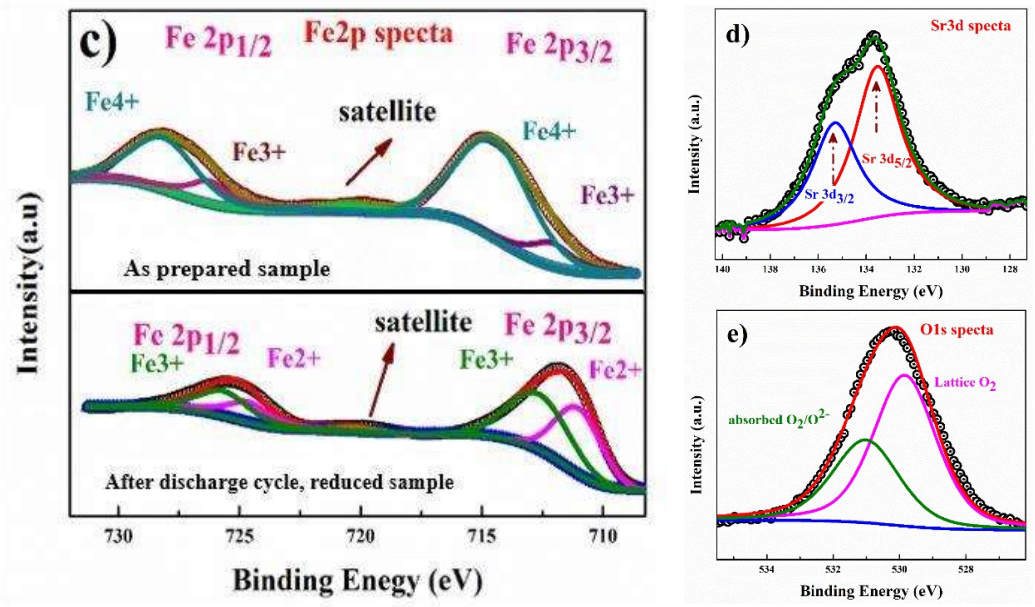


**Figure 6.1** The core-level XPS of **(c)** Fe2*p*, **(d)** Sr3*d* and **(e)** O1*s* spectrum

which is consistent with our iodometry result. The core-level regions of Sr 3*d* for Fig. 6.1d**,** and O 1*s* for Fig. 1e**,** fitted with a single chemical state suggesting that these elements are present in their single oxidation state; the elemental composition from XPS quantification was found close to 1:1:3 for $SrFeO_{3-\delta}$.

**Table 6.1** Binding energies (in eV) for XPS core-level main peaks

| | Core levels | Position (eV) | $Fe^{4+}$:$Fe^{3+}$ (%) |
|---|---|---|---|
| Before charge–discharge $Fe^{4+}$ | Fe $2p_{3/2}$ | 712.3 | 93:7 |
| $Fe^{3+}$ | Fe $2p_{1/2}$ | 726.2 | |
| | 'Shake-up' satellite | 718.28 | |
| | Fe $2p_{3/2}$ | 709.93 | |
| | Fe $2p_{1/2}$ | 723.78 | |
| After charge–discharge | Fe $2p_{3/2}$ | 710.4 | |
| $Fe^{3+}$ | Fe $2p_{1/2}$ | 723.29 | |
| | Satellite peak | 717.87 | |
| $Fe^{2+}$ | Fe $2p_{3/2}$ | 708.73 | |
| | Fe $2p_{1/2}$ | 722.18 | |
| $Sr^{2+}$ | Sr $3d_{5/2}$ | 133.5 | |
| | Sr $3d_{3/2}$ | 135.3 | |
| $O^{2-}$ | Lattice $O_2$ | 529.84 | |
| | Absorbed $O_2/O^{2-}$ | 531.01 | |

### 6.3.3 BET-Surface Area Analysis

$N_2$ adsorption-desorption isotherms with pore-size distribution is shown in Fig. 6.1f.

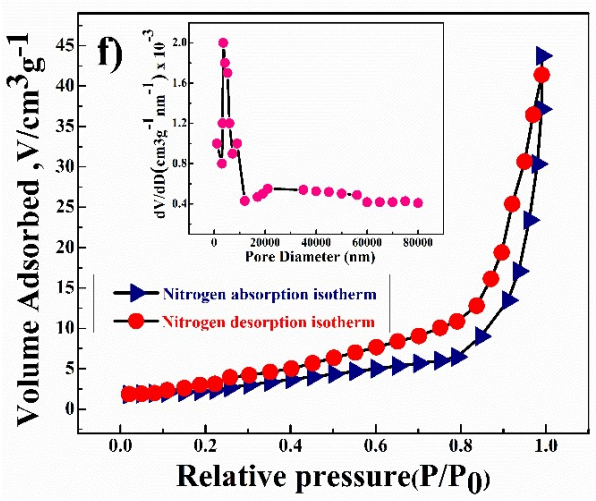


**Figure 6.1 (f)** BET surface area $N_2$ adsorption-desorption isotherms with pore-size distribution.

The linear low-pressure portion and middle section of the isotherm could be attributed to the unrestricted mono- or multilayer adsorption, suggesting that the samples possessed a blend of mesoporous and macroporous structures. The surface area for

$SrFeO_{3-\delta}$ was found to be 37 $m^2/g$ containing a large number of pores with a pore size (diameter) distribution in the range of 27 to 54 nm.

### 6.3.4 Structure, FE-SEM and HR-TEM Analysis

Fig. 6.2a shows Supercell (2×2×2) structure of stoichiometric- $SrFeO_{3-\delta}$ in cubic-perovskite structure. Fig. 6.2b, shows (110) plane containing $Sr^{2+}$, $Fe^{4+,}$ and $O^{2-}$ ions. Fig. 6.2c, shows (111) plane containing only $Fe^{4+}$ ions. Blue, dirty yellow and red balls correspond to Sr, Fe and O ions. A scanning electron micrograph (SEM) shows that the morphology of the titular compound consists of agglomerates of micron-sized crystallites (Fig. 6.2d). A high-resolution transmission electron micrograph (HRTEM) of the as-prepared $SrFeO_{3-\delta}$ powder sample depicted the presence of lattice fringes with *d*-spacing 2.72 Å, which corresponds to reflection

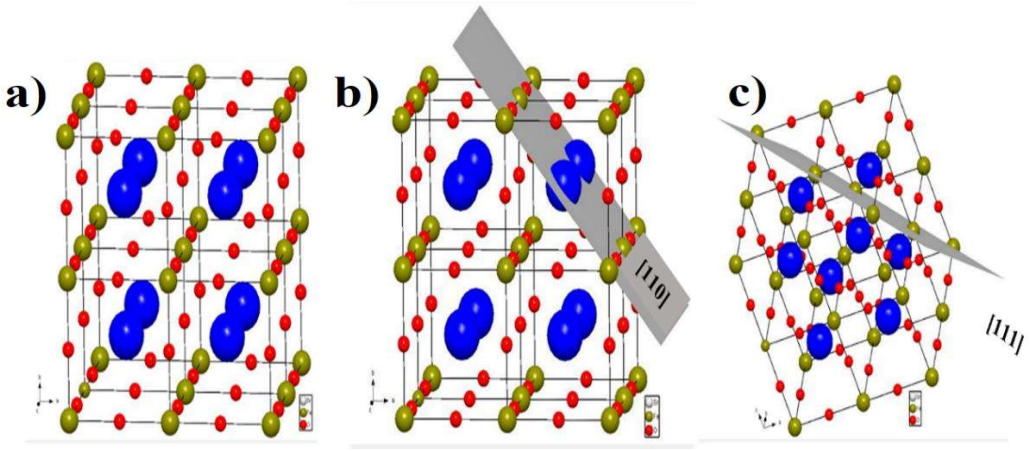


**Figure 6.2 (a)** Supercell (2x2x2) structure of stoichiometric-SrFeO3 in cubic-perovskite structure, **(b)** (110) plane containing $Sr^{2+}$, $Fe^{4+}$ and $O^{2-}$ ions and **(c)** (111) plane containing only $Fe^{4+}$ ions. Blue, green and red balls correspond to Sr, Fe and O ions.

from (110) (the highest intensity peak observed in the powder-XRD pattern). We further carried our elemental analysis by EDX of the as-prepared $SrFeO_{3-\delta}$ powder samples. EDX mappings presented in Fig. 6.3(a-d) shows that the elements Fe and Sr are uniformly distributed.

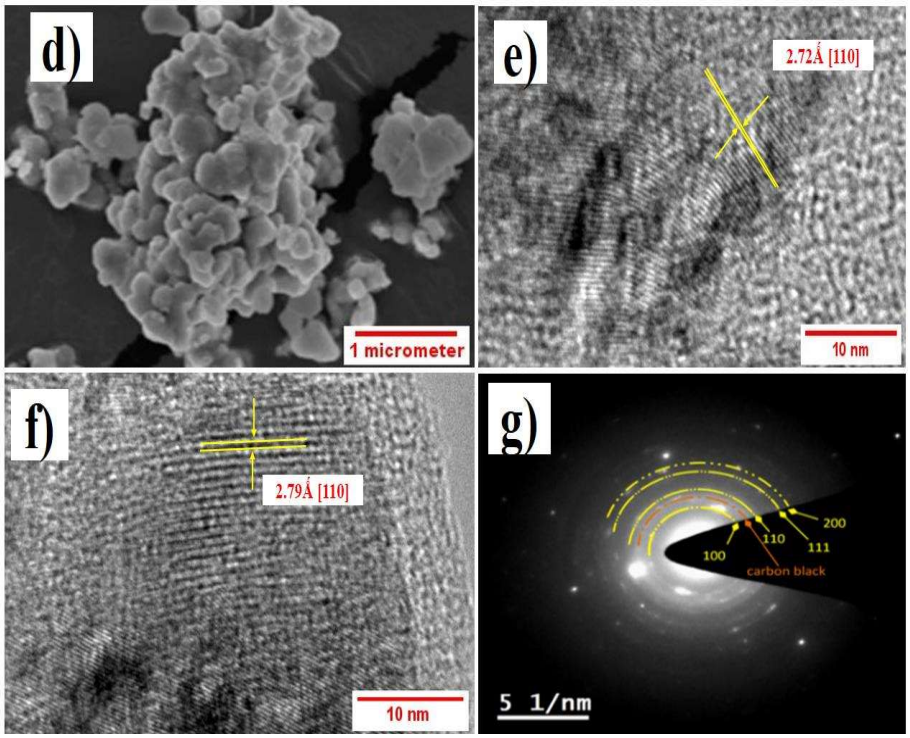


**Figure 6.2 (d)** SEM images of as-prepared $SrFeO_{3-\delta}$, **(e, f)** HRTEM images of as-prepared $SrFeO_{3-\delta}$ showing lattice fringes with *d*-spacing corresponding to (110) plane before and after the complete discharge cycle and **(g)** Selected area electron diffraction (SAED) pattern of the sample after complete discharge cycle.

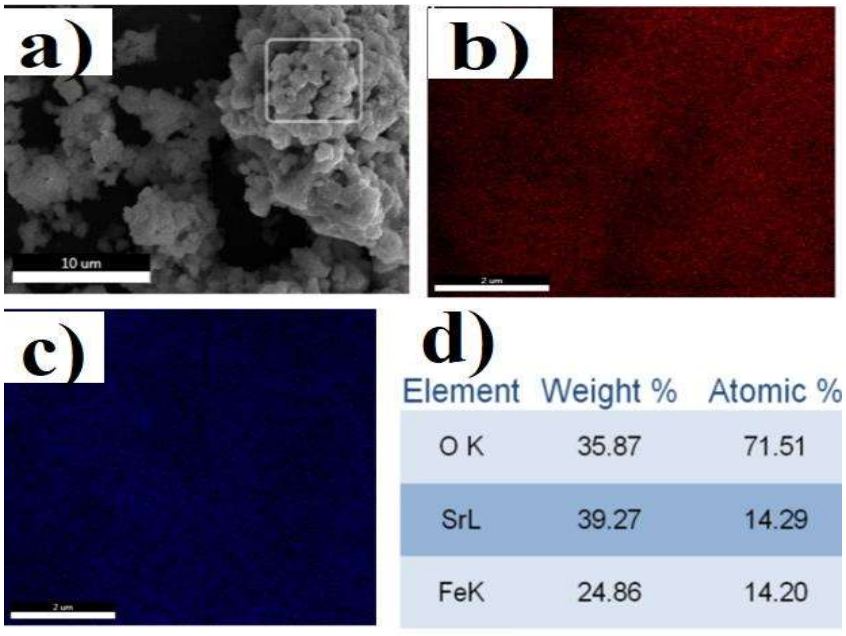


**Figure 6.3 (a)** SEM image of the area of interest, **(b)** Sr map, **(c)** Fe map and **(d)** Elemental analysis showing Fe: Sr ratio the as-prepared powder sample of $SrFeO_{3-\delta}$.

### 6.3.5 Electrochemical Studies:

#### 6.3.5.1 Cyclic Voltammetry Analysis

The charge-storage capacity of the $SrFeO_{3-\delta}$ composite-electrodes was first evaluated by cyclic voltammograms (CV) in a three-electrode system. The CV curves were measured for different concentrations of KOH, namely 0.1, 0.5, 1, 2, 5 and 6 M. From the KOH concentration vs. mass specific capacitance plot depicted in Fig. 6.4a, the mass-specific capacitance was calculated by eq. 6.1, mass specific capacitance are 297, 385, 492, 733, 307 and 221 F $g^{-1}$ respectively at 1 $mVs^{-1}$ in 0.1, 0.5, 1, 2, 5 and 6 M KOH. The specific capacitance initially increases with increasing $OH^-$ concentration, attains the highest capacitance for 2 M KOH solution and then decreases on further increasing the $OH^-$ concentration.

$$C = \frac{\int_{E_1}^{E_2} i\,(E)dE}{2\,m\,v\,(E_2 - E_1)} \qquad (6.1)$$

where $C$ is the capacitance in F/g; ($E_2$–$E_1$) is the width of the potential window (V), $i\,(E)$ is the instantaneous current (A); integral $\int_{E_1}^{E_2} i\,(E)dE$ is the total voltammetric charge obtained by integration of both positive and negative sweeps in a CV and hence factor ½ is used to calculate charge in either forward or backward scan; $m$ is the mass (g) of active material; $v$ is scan rate (V/s).

The shape of the CV curve changes with KOH concentration is shown by the typical CV curves given in Fig. 6.4b-e. At lower KOH concentrations (Fig. 6.4b and c), the CV curves have a quasi-rectangular shape indicating that $SrFeO_{3-\delta}$ electrode exhibits both pseudocapacitive and double-layer capacitive behavior at lower $OH^-$ concentrations. As the concentration of $OH^-$ ion is increased (Fig. 6.4d, e), the CV curves display non-rectangular

behavior indicating that pseudocapacitive behavior dominates over EDLC at higher $OH^-$ concentrations. With the 0.1 M KOH electrolyte (Fig. 6.4b), two redox-reaction peaks are easily discernible at -0.88 and -0.25 V (note that all the potentials are reported vs Hg/HgO (1 M KOH) reference electrode) and with increasing KOH concentration, the separation between the anodic and cathodic peaks becomes

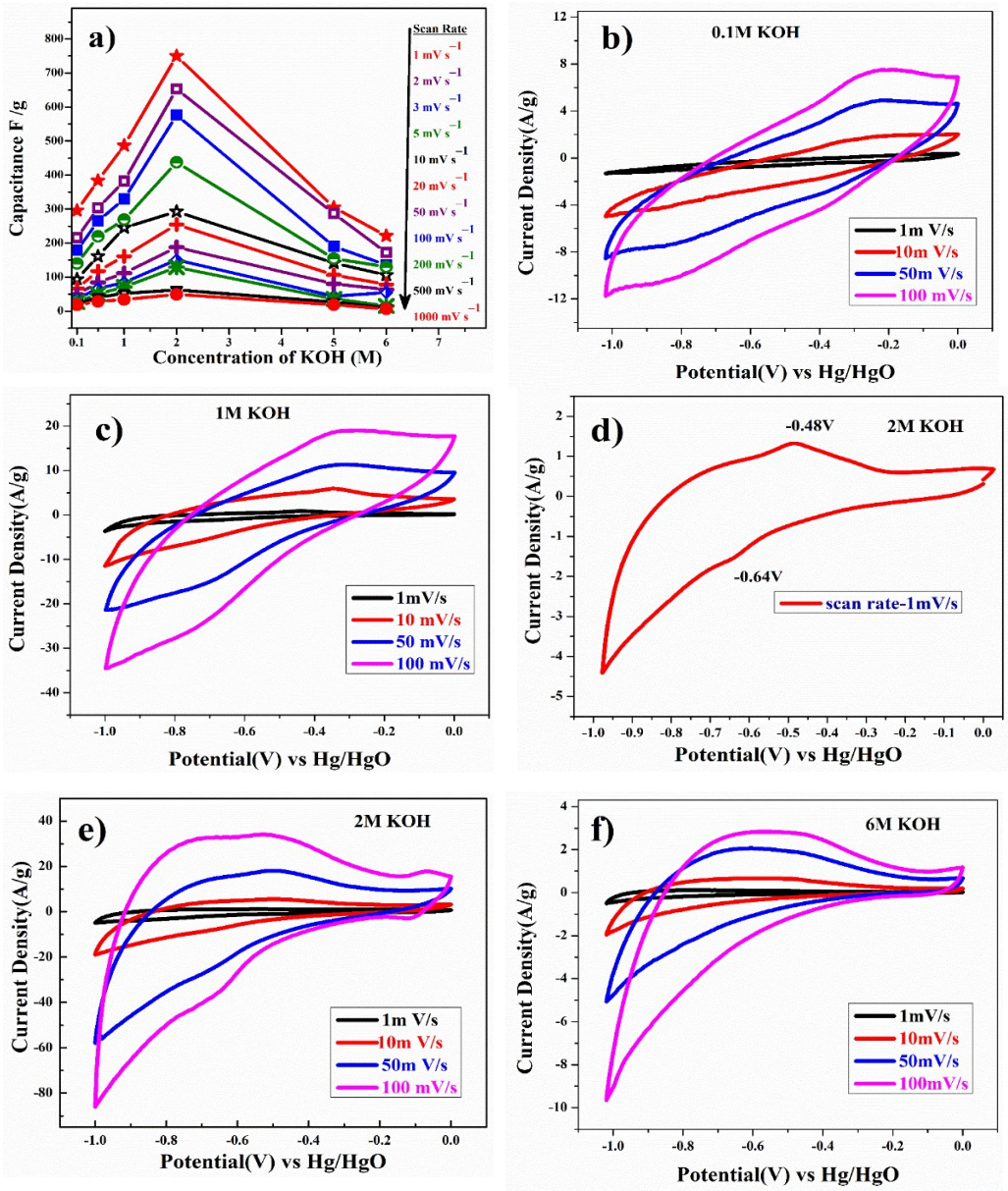


**Figure 6.4 (a)** KOH concentrations vs specific capacitance at different scan rates. Typical CV curves for $SrFeO_{3-\delta}$ in **(b)** 0.1 M, **(c)** 1 M, **(d)** 2 M @ 1mV/s, **(e)** 2 M and **(f)** 6 M KOH solution at different scan rates of 1, 10, 50 and 100 mV/s.

narrower, as indicated in Fig. 6.4c-e, suggesting better reversibility of redox reactions with increasing KOH concentration. On further increasing the KOH concentration beyond 2 M, these redox reaction peaks are no longer discernible in the CV curves (Fig. 6.4f). No shift in the redox reaction peaks are observed with increasing scan rate, indicating polarization of the electrode does not occur at higher scan rates owing to the good electrical conductivity of $SrFeO_{3-\delta}$.

In the voltage window of 1 V, the theoretical capacity of $SrFeO_{3-\delta}$ is 504 F $g^{-1}$ with $1e^-$ charge transfer coupled with intercalation of $OH^-$ ions. In our study, $SrFeO_{3-\delta}$ displayed a stable capacitance equivalent to 733 F $g^{-1}$. This suggest at least transfer/exchange of 1.45 $e^-/OH^-$ per $SrFeO_{3-\delta}$ molecule suggesting the participation of both $Fe^{4+/3+}$ and $Fe^{3+/2+}$ redox couples in charge storage. As $SrFeO_{3-\delta}$ contains almost 92% of iron in +4 oxidation state and 8% in +3 oxidation state, the redox reaction for high capacitance of $SrFeO_{3-\delta}$ can be represented as

$$\mathbf{Sr[Fe^{4+}_{0.92}\,Fe^{3+}_{0.08}]\,O_{2.96} + 1.45e^- + 0.725H_2O} \quad \updownarrow \quad \mathbf{Sr[Fe^{3+}_{0.47}\,Fe^{2+}_{0.53}]O_{2.235}\,.(OH^-)_{1.45}} \qquad (6.2)$$

### 6.3.5.2 Kinetics Studies and Trassati's Plot Analysis

The charge storage mechanism is evaluated by the faradic (intercalation/de-intercalation reaction and charge transfer reaction) and non-faradic contribution (electric double-layer effect at electrode/electrolyte interface). [36, 37] The high specific capacitance of $SrFeO_{3-\delta}$ is attributed to both diffusion-controlled and non-diffusion-controlled (surface control redox mediated pseudocapacitance) processes. To evaluate the contribution of diffusion-controlled and non-diffusion-controlled (surface control EDLC and pseudocapacitance) capacitance with respect to the experimental data, Trasatti [38] and Dunn [39] methods are adopted.

The total charge stored in the inner and outer surface of the material is estimated by the Trasatti's plot shown in Fig. 6.5a, b. The charge storage mechanism is dependent on the scan rate from CV analysis. The surface redox reaction and charge accumulation between active material and electrolyte help in estimating the total charge storage by eq. 6.3.

$$C_{Total} = C_{dl} + C_{pseudo} \quad (6.3)$$

Where, $C_{Total}$ is the total capacitance, which contain $C_{dl}$ (double layer capacitance) and $C_{pseudo}$ (pseudocapacitance), while the total charge is attributed mostly at outer surface with higher scan rate. Therefore, the accurate inner and outer charge contribution can be evaluated only at lower scan rates. The outer charge or total capacitance contribution is estimated by using eq. 6.4.

$$C^{-1}(\upsilon) = C_{Total} + constant(\upsilon^{0.5}) \quad (6.4)$$

Where, υ is the scan rate formed by the linear fitting of $C^{-1}(\upsilon)$ versus $\upsilon^{0.5}$ given in Fig. 6.5a, the total capacitance $C_{Total}$, which is 733 F $g^{-1}$ in the present study. Thus at the outer surface of the electrode material, the amount of charge stored is obtained by extrapolating the graph to the y-axis ($C(\upsilon)$ versus $\upsilon^{-0.5}(\upsilon)$ presented in Fig. 6.5b) and the double-layer capacitance value is found to be 223 F $g^{-1}$ of total capacitance using eq. 6.5.

$$C(\upsilon) = C_{dl} + constant(\upsilon^{-0.5}) \quad (6.5)$$

From eq. 6.3, the amount of charge that is stored in the inner surface (pseudocapacitance) is calculated to be 510 F $g^{-1}$. From the above results, it could be concluded that the total capacitance contribution from the non-diffusion-controlled

outer surface (surface controlled redox mediator capacitance) is almost ~30%, while the inner surface contribution is ~70%.

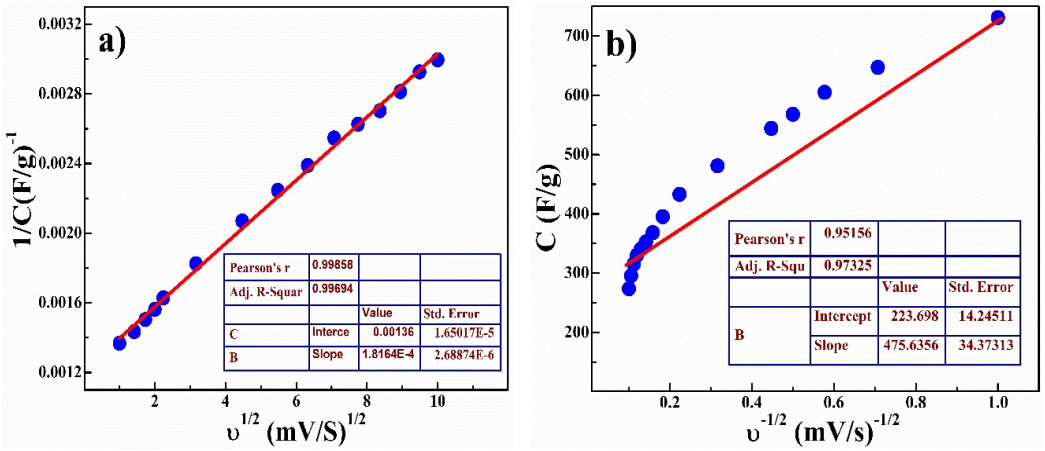


**Figure 6.5 (a, b)** Plot showing the total capacitance $C_{Total}$ and amount of charge stored at the outer surface $C_{dl}$ estimated by the Trassati plot.

### 6.3.5.3 Determination of Diffusion Coefficient and Dunn's Plot Analysis

Similarly, according to the Dunn method, the total charge storage in the $SrFeO_{3-\delta}$ material is evaluated. Herein, the diffusion-controlled and non-diffusion-controlled (surface control pseudocapacitance and EDLC) processes contribution is obtained by analyzing CV data at different scan rates from 1 to 100 mV $s^{-1}$. The relationship between the scan rate (ν) and measured current (I) concluded the degree of capacitive effect from the CV data (eq. 6.6).

$$I(V) = a\upsilon^{b} \tag{6.6}$$

$$\log_{10} I(V) = \log_{10} a + b \log_{10} \upsilon \tag{6.7}$$

where, parameters $a$ and $b$ are adjustable. The b value obtained from the slope of $\log_{10} I(V)$ vs. $\log_{10}$ υat the cathodic (-0.8 V) and anodic peak potential (-0.7 V) shown in Fig. 6.5c. Theoretically, when $b$ value is 0.5, then CV current obeys Cottrell's equation ($I = a\upsilon^{0.5}$) having an intercalation/de-intercalation mechanism, and when $b$

value is 1, then CV current obeys capacitive mechanism. Herein, *b* values were found to be 0.72 and 0.73 for cathodic and anodic peaks respectively, suggesting that CV current is a linear combination of diffusion and pseudocapacitive contributions (redox mediator process) behavior. Furthermore, *b* values have been evaluated at different potentials (as shown in Fig. 6.5d and inset) and they were found to be in the range of 0.6 to 0.7 for the cathodic sweep, which corroborates the majority of capacitance arises from diffusion-controlled processes. The current response is directly proportional to the scan rate (according to eq. 6.8). [36, 39]

$$i_p = 2.686 \times 10^5 \times n^{3/2} A D^{1/2} C_o v^{1/2} \qquad (6.8)$$

where, $i_p$ is peak current (A), $n$ is number of electrons transferred in the redox event, $A$ ($cm^2$)is electrode area, $D$ ($cm^2/s$) is diffusion coefficient, $C_o$ ($mol/cm^3$) is $OH^-$ ion concentration, $v$ (V/s) is scan rate. Further $OH^-$ diffusion coefficients were calculated using eq. 6.8 at 1mV/s of $SrFeO_{3-\delta}$ electrode is $5.476 \times 10^{-13}$ $cm^2/s$ represent to cathodic peak current.

$$I = \upsilon C_T A \qquad (6.9)$$

Where $C_T$ is the capacitance and from Fig. 6.5d**,** the obtained b value was found to be ~0.6 at various potentials. Following the above concept, the graph of the square root of the scan rate $\upsilon^{0.5}$versus $I/\upsilon^{0.5}$ is plotted at a fixed potential to study the diffusion-controlled and non-diffusion-controlled (surface control) processes for the charge storage mechanism as given in eq. 6.9 and eq. 6.10.

$$I(\upsilon) = K_1\upsilon + K_2\upsilon^{0.5} \qquad (6.10)$$

The current contributions from the capacitive and diffusion control are $K_1\upsilon$ and $K_2\upsilon^{0.5}$ respectively. Then, by dividing by $\upsilon^{0.5}$, eq. 6.10 will be as eq. 6.11.

$$I/\upsilon^{0.5} = K_1\upsilon^{0.5} + K_2 \qquad (6.11)$$

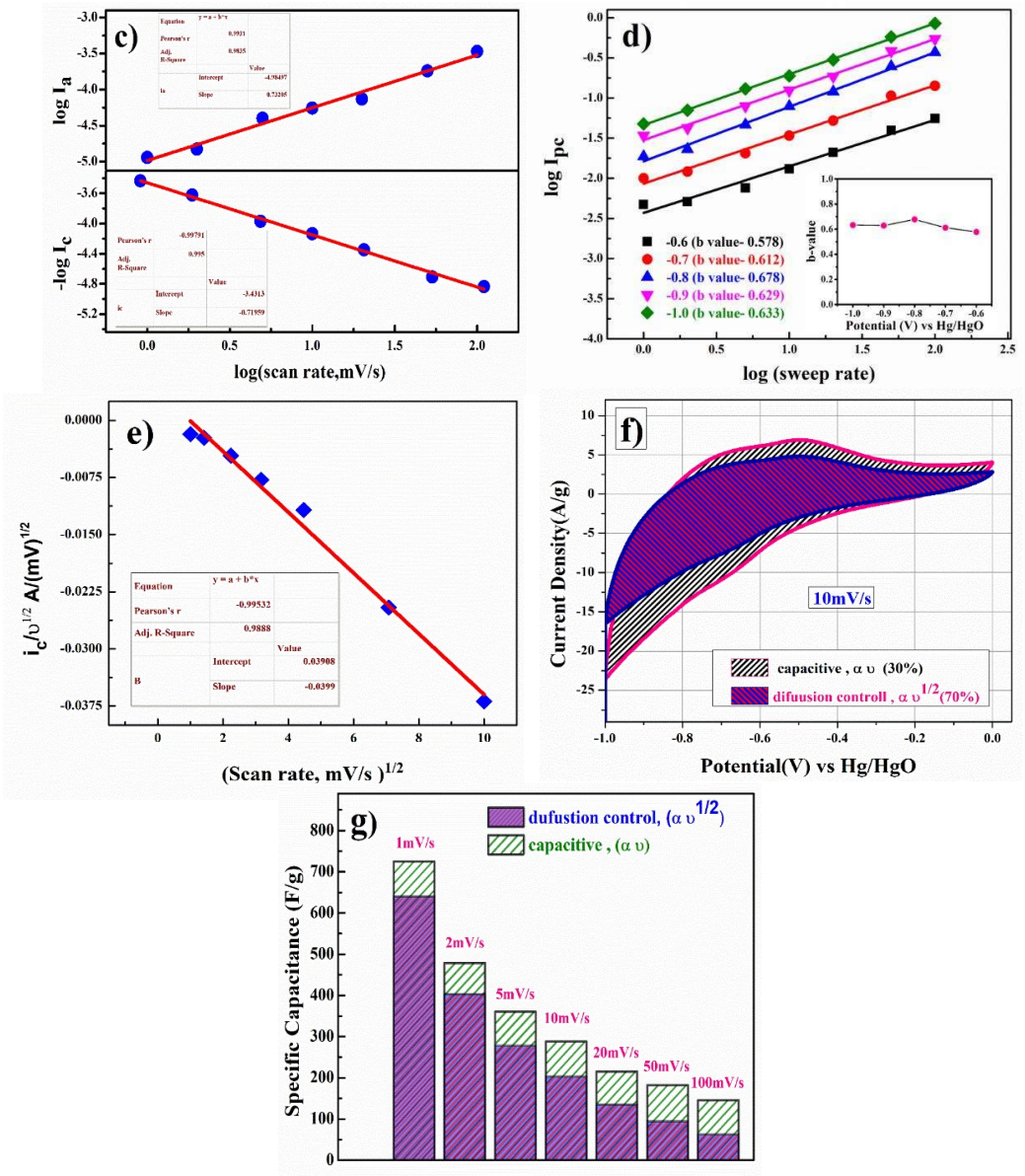


**Figure 6.5 (c)** The slope of $\log_{10} I(V)$ vs. $\log_{10}$ υ shows b value at the cathodic (-0.8 V) and anodic peak potential (-0.7 V), **(d)** b value plot at various potentials, **(e)** $K_1$ and $K_2$ values are obtained from Dunn's method, **(f)** Plot showing the capacitive contribution (white shaded area) and diffusion-controlled process (red-pink line shaded area) at a scan rate of 10 mV $s^{-1}$ and **(g)** Capacitive contributions at different scan rate.

### 6.3.5.4 Charge/Discharge Analysis and Cyclic Stability Test

Pseudocapacitors typically lose capacitance on repeated cycling due to the sluggish charge transfer reaction, [7, 17] therefore, to assess the electrochemical stability of $SrFeO_{3-\delta}$ electrodes, 2500 repeated CV cycles were performed at a scan rate of 100 mV/s. We observed a slight increase (<3%) in the capacity retention within the first 500 cycles which is attributed to minor re-orientation of $SrFeO_{3-\delta}$ crystallites during the electrochemical testing in agreement to our HRTEM analysis (in the following paragraph) where it is observed that iron-containing (111) plane of $SrFeO_{3-\delta}$ became preferentially oriented within crystallites of the composite electrode. After 500 cycles, the capacitance retention is largely stabilized and a loss of < 7% capacitance retention was observed after 2500 cycles, indicating excellent cyclability of this perovskite material, a pre-requisite for any promising supercapacitor electrode. The GCD behavior was also investigated, Fig. 6.6a, by chronoamperometry at different current densities ranging from 1 to 10 A $g^{-1}$. The discharge curves show a sudden potential drop followed by a slow potential decay which is a characteristic of typical pseudocapacitive behavior. The mass specific capacitance from the charge-discharge plot was calculated using the eq. 6.12.

$$C = \frac{It}{m(E_2 - E_1)} \qquad (6.12)$$

where $C$ is the capacitance in F/g, $I$ is constant discharge current applied in a GCD scan in amperes(A), ($E_2$–$E_1$) is the width of the potential window applied in volts (V), $m$ is the mass of active material in grams(g) and $t$ is the total discharge time in seconds(s).

The capacitance of $SrFeO_{3-\delta}$ was found to be 743, 598, 481, 416 and 307 $Fg^{-1}$ respectively at 1, 2, 3, 5 and 10 A $g^{-1}$ respectively which demonstrate good capacitance retention during repeated charge-discharge cycling as indicated in Fig.

6.6b. Fig. 6.6c**,** shows 92% capacitance retention after 2500 charge-discharge cycles with 94% Coulombic efficiency (with inset of GCD 2500 cycles at 10 A $g^{-1}$ current density).

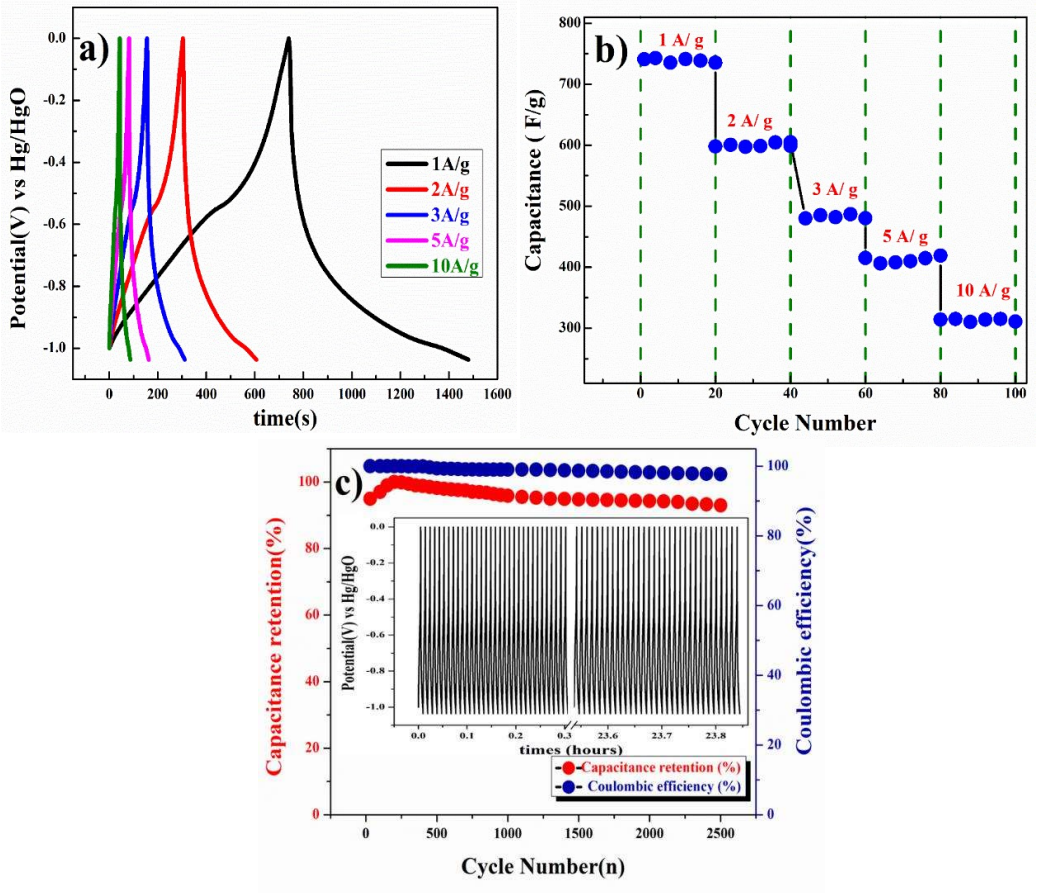


**Figure 6.6 (a)** Galvanostatic charge/discharge curves measured with different current densities in 2 M KOH, **(b)** Cycle number versus capacitance from GCD at different current densities and **(c)** Capacitance retention and coulombic efficiency plot of $SrFeO_{3-\delta}$

### 6.3.5.5 Analysis of Electrochemical Impedance Spectroscopy (EIS)

The Nyquist plots, Fig. 6.6d, obtained at two different applied potentials exhibit a negligible semicircle in the high-frequency region, representing a low interfacial charge-transfer resistance across the electrode/electrolyte for the faradaic reactions again attributed to good electrical conductivity of $SrFeO_{3-\delta}$ electrode. The Rs and Rct value is $SrFeO_{3-\delta}$ is found to be 1.26 Ω and 0.29 Ω respectively (see the enlarged view

in the inset of Fig. 6.6d). The straight line in the low-frequency region is an indication of good diffusion-controlled process. EIS spectra after 2500 repeated charge-discharge cycles with the first, inset of Fig. 6.6d, demonstrating the good electrochemical stability of $SrFeO_{3-\delta}$ electrode.

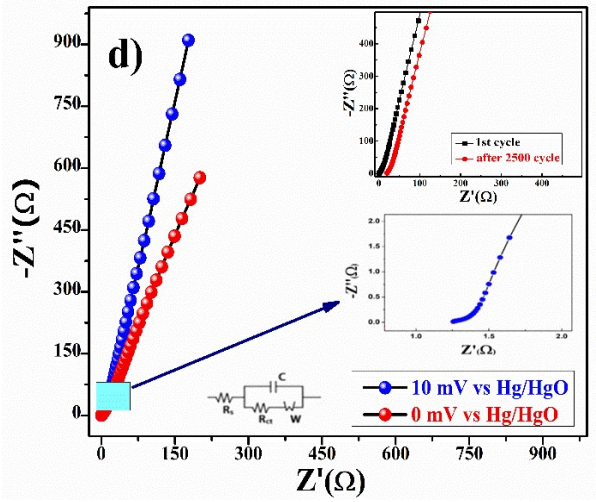


**Figure 6.6 (d)** Impedance spectra measured at 0 and -0.4V in a three-electrode configuration in 2 M KOH; inset compares the impedance spectra obtained after cycle 1 and 2500 of repeated charge discharge scans.

### 6.3.5.6 Structural Stability Test

In order to further investigate the long-term structural stability of $SrFeO_{3-\delta}$ electrode during electrochemical testing, after 2500 charge-discharge cycles, the material was undergone for reduction or discharge cycles and active electrode materials ($SrFeO_{3-\delta}$) was extracted from the electrode and studied by HRTEM and XPS studies to investigate the status of the crystal and electronic structure of the material. HRTEM image (see Fig. 6.2g), also show the change in the *d* spacing of lattice fringes also from 2.72 to 2.79 Å. Fig. 6.2h, show the SAED image representing the diffraction rings corresponding to the diffraction peaks obtained in the XRD pattern of the starting material. An additional ring between (100) and (110) planes is attributed to acetylene black carbon used in making the composite electrode for an electrochemical test; other

than this ring, no other diffraction ring was observed suggesting the absence of any other impurity phases implying that the crystal structure of parent $SrFeO_{3-\delta}$ remains intact even after 2500 cycles of CV testing. XPS study of Fe(2*p*) core level after a complete discharge cycle of the electrode was carried out.

XPS plot is presented in Fig. 6.1c show that Fe ion exist in $Fe^{3+}$ (53%) and $Fe^{2+}$ (47%) in the discharged or reduced sample. The study matches well with our proposition behind high electrochemical capacitance of the materials.

### 6.3.5.7 Asymmetric Full Cell Test of $SrFeO_{3-\delta}$ //AC (CV, GCD and Cyclic Stability)

To explore the real applicability of the $SrFeO_{3-\delta}$ electrode, the two-electrode full cell was fabricated in asymmetric supercapacitor cell (ASC) mode in a 2 M KOH electrolyte where AC was employed as a positive electrode. To determine the maximum specific capacitance during the full-cell test, the storage capacities of the positive and negative electrodes must be balanced using eq. 6.13.

$$\frac{1}{C_{total}} = \frac{1}{C_{positive}} + \frac{1}{C_{negative}} \qquad (6.13)$$

Equation 6.14 determines the mass ratio (m+/m-) of the positive and negative electrode materials to balance the cell's capacity to store charges.

$$\frac{m^+}{m^-} = \frac{C_- \times \Delta E_-}{C_+ \times \Delta E_+} \qquad (6.14)$$

where, $m^+$,$m^-$, $C_+$, $C_-$, $\Delta E_+$, $\Delta E_-$ are mass loading on the electrode, specific capacitance, and potential window of positive and negative electrodes estimated by single electrode measurements.

With a fixed scan rate (10 mV/s), separate CV curves for the AC (positive electrode) and $SrFeO_{3-\delta}$ (negative electrode) are shown in Fig. 6.7a with a single operating potential window range. The contribution in capacitance due to the AC electrode is extracted when calculating the electrochemical charge storage capacity of the $SrFeO_{3-\delta}$

electrode because AC is used to increase the conductivity of the active electrode. Thus the obtained data shows only the capacitive value of the $SrFeO_{3-\delta}$ electrode. For the asymmetric cell, the calculated mass ratio ($m^+/m^-$) was 1.9:1, and the active material's weight was found to be ~3.6 mg (excluding the weight of activated carbon and PVDF). Fig. 6.7b shows the CV plot of two-electrode asymmetric supercapacitor cell (ASCs) $SrFeO_{3-\delta}$//AC, at scan rates ranging from 1 to 100 $mVs^{-1}$ in the potential window -1 to 1 V. Fig. 6.7c depicts the full cell's galvanostatic charge/discharge profile at different current densities. The specific capacitances of ASCs calculated from GCD curves were found to be 344.0, 260.6, 176.0, 109.5 and 66.5 F/g at constant current densities of 1, 2, 3, 5 and 10 A/g, respectively.

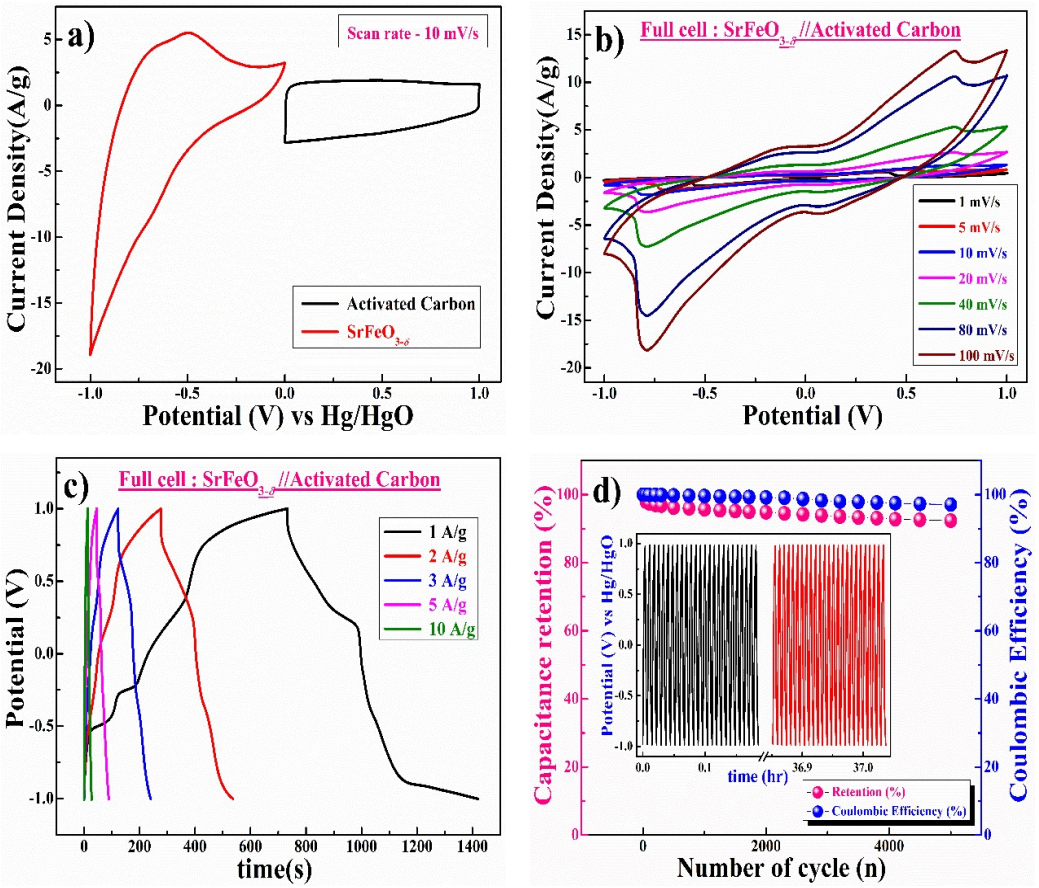


**Fig. 6.7 (a)** Separate CV plots for activated carbon and $SrFeO_{3-\delta}$ electrode in 2 M KOH Electrolyte 10 mV/s, **(b)** CV at different scan rates, **(c)** Charge-discharge at different current rates, and **(d)** Capacitance retention and coulombic efficiency.

The $SrFeO_{3-\delta}$//AC full cell, as shown in Fig. 6.7d, has exceptional long-term cycling stability, with 92.4% capacity retention after 5000 cycles. Further, after 5000 cycles, the $SrFeO_{3-\delta}$//AC

full cell's coulombic efficiency has lost merely 3% of its initial value.

**6.3.5.8 Electrochemical Impedance Spectroscopy (EIS) of $SrFeO_{3-\delta}$//AC Full Cell**

Fig. 6.7e shows the Nyquist plot at an open circuit potential in the frequency range of 100 kHz to 0.1 Hz, confirming the superior charge transfer, higher specific capacitance and excellent retention of the electronic structure of the $SrFeO_{3-\delta}$//AC full cell in ASC mode. However, a slight reduction in capacity is due to the partially irreversible nature of the electrode, which was shown during the cycling test. The EIS result corroborates the evidence for cycling stability by demonstrating a slight difference in the cell's internal and charge transfer resistances before and after the cycling test.

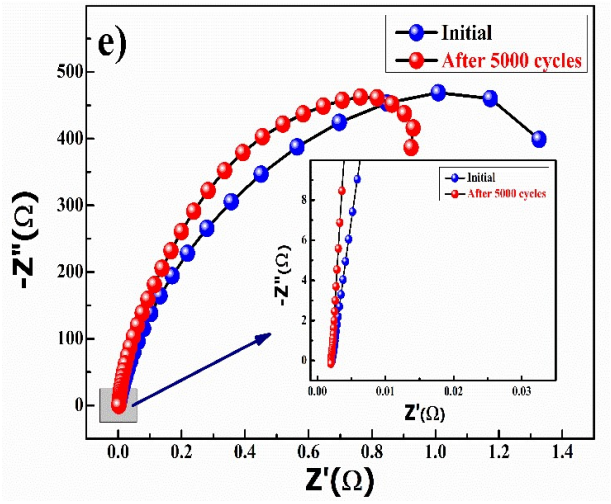


**Fig. 6.7 (e)** Nyquist at 10 mV at initial cycle and after 5000 cycles of full cell formation.

**6.3.5.9 Study of Energy Density vs Power Density of $SrFeO_{3-\delta}$//AC Full Cell**

Equations 6.15 and 6.16 were utilized to calculate the power and energy density of the ASC.

$$P(W/kg) = \frac{E \text{ X } 3600}{t_{dis}} \qquad (6.15)$$

$$E(Wh/kg) = \frac{1}{2}\frac{C_{ASC}}{3.6}\Delta V^2 \qquad (6.16)$$

where $C_{sp}$ is specific capacitance, ΔV is the operating voltage window, and $t_{dis}$is discharge time. Fig. 5.10g displays the Ragone plot (energy density vs. power density) of the $SrFeO_{3-\delta}$//AC full-cell compared to earlier reported metal oxide-based and other supercapacitors.

The ASC resultant values confirm the highest energy density equivalent of 191 Wh/kg and power density equivalent of 0.99 kW/kg at 1 A/g current density. When the current density was raised to 10 A/g, the maximum power density of 10.0 kW/kg was obtained and the energy density was reduced to 36.9 Wh/kg. A literature review of several metal oxide-based electrodes for supercapacitor applications, such as specific capacitance, capacity retention, energy and power density is shown in **Table 6.2**.

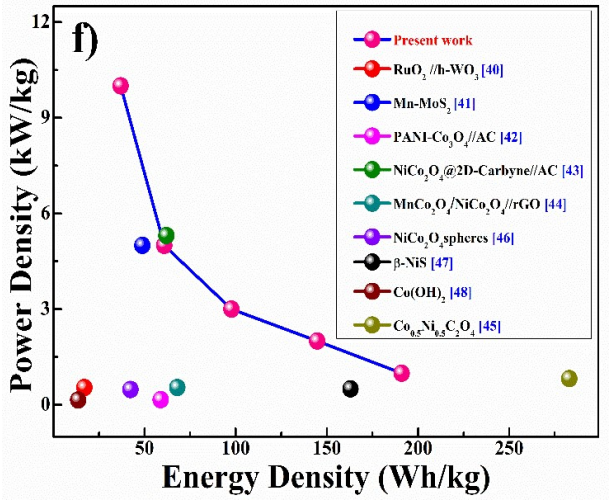


**Fig. 6.7 (f)** Ragone plot of the $SrFeO_{3-\delta}$//AC full cell in ASC mode in comparison with reported supercapacitor devices.

$SrFeO_{3-\delta}$ has attracted considerable attention in the recent past due to their exciting and technologically useful structural, magnetic and electrical properties. The unusual valence of $Fe^{4+/3+}$ in $SrFeO_{3-\delta}$ makes it an oxygen-deficient compound resulting in metal-like conductivity and depending on the extent of oxygen vacancy, the structure assumes a tetragonal (δ = 0.13), orthorhombic (δ = 0.27) and brown-millerite (δ = 0.5)

phases. From iodometry and XPS analysis, it was deduced that $SrFeO_{3-\delta}$ exist as $SrFe^{4+}_{0.92}Fe^{3+}_{0.08}O_{2.96}$ and therefore, $H_2O/OH^-$ anions intercalation/deintercalation of the aqueous electrolyte phase became responsible for high pseudocapacitance of the material.

**Table 6.2.** Displays the Ragone plot of the $SrFeO_{3-\delta}$//AC (ASC) full cell compared with reported supercapacitor devices.

| Material | Energy density (Wh/kg) | Power density (kW/kg) | Cycling stability (%) after "n" cycles | Capacitance (F/g) | Ref. |
|---|---|---|---|---|---|
| $RuO_2$//h-$WO_3$ | 16.92 | 0.54 | 171.7%, 6500 | 47.6 at 0.68 A/g | [40] |
| Mn/$MoS_2$ | 48.80 | 5.00 | 77.0%, 5000 | 88 at 1 A/g | [41] |
| PANI-$Co_3O_4$//AC | 58.84 | 0.16 | 74.8%, 3000 | 298.4 at 0.3 A/g | [42] |
| $NiCo_2O_4$@2D-Carbyne//AC | 62.00 | 5.31 | 81.0%, 3000 | 125.5 at 1 A/g | [43] |
| $MnCo_2S_4$/ $NiCo_2S_4$//rGO | 68.00 | 0.54 | 86.4%, 5000 | 192 at 1 A/g | [44] |
| $Co_{0.5}Ni_{0.5}C_2O_4$ | 283 | 0.82 | 90.7%, 2500 | 796 F/g at 1 A/g | [45] |
| $NiCo_2S_4$ spheres | 42.3 | 0.48 | 78.6%, 10000 | 119.1 at 5 mV/s | [46] |
| β-NiS | 163 | 0.5 | 90.0%, 2500 | 780 at 1 A/g | [47] |
| $Co(OH)_2$ | 13.6 | 0.15 | 80.0%, 5000 | 38.9 at 2 A/g | [48] |
| **$SrFeO_{3-\delta}$//AC** | **191.0<br>144.7<br>97.7<br>60.8<br>36.9** | **0.99<br>2.0<br>3.0<br>5.0<br>10.0** | **93.0%, 5000** | **344 at 1 A/g** | **Present work** |

## 6.4 Conclusions

Non-stoichiometric nominal $SrFeO_{3-\delta}$ perovskite oxide was successfully synthesized using a molten salt flux method with potassium hydroxide as the flux; formation of the perovskite phase was confirmed using XRD, XPS, SEM and TEM study. $SrFeO_{3-\delta}$ electrode in 2 M KOH aqueous electrolyte proves to be an excellent negative electrode for a faradaic electrochemical capacitor

cycled between 0 to -1 V versus Hg/HgO (1 M KOH) reference electrode offering pseudocapacitive behavior with a specific capacitance of *ca*. 733 F $g^{-1}$ at a scan rate of 1 mV/s for CV scans and *ca*. 743

**Table 6.3** Values of specific capacitance of some transition-metal oxides. Nano-structured materials and carbon/graphene-modified oxide materials are excluded from the list for the likeness of comparison of common transition-metal oxides with $SrFeO_{3-\delta}$.

| Material | Capacitance (F $g^{-1}$) | Current Density or Scan Rate | Electrolyte | Reference |
|---|---|---|---|---|
| $RuO_2$. $nH_2O$ | 720 | - | Strong $H_2SO_4$ | [49] |
| $\alpha$-$MnO_2$ | 297 | 0.5 mA/$cm^2$ | 0.1 M $Na_2SO_4$ | [50] |
| $\beta$-$MnO_2$ | 9 | 0.5 mA/$cm^2$ | 0.1 M $Na_2SO_4$ | [50] |
| porous NiO | 50 | 20 mV/s | 1 M KOH | [8] |
| Amorphous $V_2O_5$ | 350 | 2 mA/$cm^2$ | 2 M KCl | [10] |
| $Co_3O_4$ | 746 | 5 mA/$cm^2$ | 6 M KOH | [11] |
| $Fe_3O_4$ | 170 | 2 mV/s | 1 M $Na_2SO_3$ | [51] |
| porous$NiCo_2O_4$ | 1089 | 2 A/g | 2 M KOH | [14] |
| doped-$SrRuO_3$ | 160 | 20 mV/s | 6 M KOH | [24] |
| $LaNiO_3$ | 160 | 10 mV/s | 1 M $Na_2SO_4$ | [27] |
| $LaMnO_{2.91}$ | 610 | 1 mV/s | 1 M KOH | [28] |
| Ni doped $Mn_3O_4$ | 704 | 10 mV/s | 1 M $Na_2SO_4$ | [52] |
| Mn-$MoS_2$ | 430 | 5 mV/s | 0.5 M $Na_2SO_4$ | [41] |
| Pyrite $FeS_2$ | 308 | 5 mV/s | 1 M $Na_2SO_4$ | [53] |
| $(Ni_{0.33}Co_{0.67})Se_2$ | 828 | 1 A/g | 3 M KOH | [54] |
| **$SrFeO_{3-\delta}$** | **733**<br>**741** | **1 mV/s**<br>**1 A/g** | **2 M KOH** | **Present work** |

F $g^{-1}$ at a current density of 1 A $g^{-1}$ for GCD scans. It also demonstrated excellent cyclability and stability at over 2500 repeated CV with capacitance retention >92% and over 94% of Coulombic efficiency. Surface capacitive and diffusion control contributions for capacitance are about 30% and 70% respectively at peak current and scan rate equivalent to 1mV/s. High gravimetric capacitance

equivalent 743, 598, 481, 416 and 307 F $g^{-1}$ respectively at 1, 2, 3, 5 and 10 A $g^{-1}$ respectively constant current was observed for $SrFeO_{3-\delta}$ electrode. Excellent pseudocapacitive performance is attributed to its good electrical conductivity, which provides fast ion and electron transfer between the electrode-electrolyte interface and the fortuitous tendency of the perovskite structure to accommodate flexible $O^{2-}/OH^{-}$ conversion in aqueous electrolyte giving rise to its good cycle-life, a pre-requisite for any promising supercapacitor electrode. The $SrFeO_{3-\delta}$ //AC full cell achieved a maximum energy density of 191 Wh/kg and a power density of 0.99 kW/kg in the 2 V voltage window in 2 M KOH electrolyte at 1 A/g current density. Results demonstrate that charge storage behavior and the capacitance value are comparable to or superior to most of the reported transition-metal nanostructured pseudocapacitors/supercapacitors. We have summarized the results of bulk/pristine transition- metal oxide (TMO) based pseudocapacitors in Table 6.3**,** for likeness of comparison with $SrFeO_{3-\delta}$ electrodes. The charge-storage pseudocapacitive behavior of $SrFeO_{3-\delta}$ and the capacitance value is comparable or superior than that of most of bulk/pristine TMOs reported to date; $SrFeO_{3-\delta}$ offers a cheap and abundant alternative to scarce and expensive $RuO_2$, a state-of-the-art pseudocapacitive material.

## 6.5 References


1. Trasatti, S. and G. Buzzanca, *Ruthenium dioxide: A new interesting electrode material. Solid state structure and electrochemical behaviour.* Journal of electroanalytical chemistry and interfacial electrochemistry, 1971. **29**(2): p. A1-A5.
2. Augustyn, V., P. Simon, and B. Dunn, *Pseudocapacitive oxide materials for high-rate electrochemical energy storage.* Energy & Environmental Science, 2014. **7**(5): p. 1597-1614.
3. Lee, H.Y. and J.B. Goodenough, *Supercapacitor behavior with KCl electrolyte.* Journal of Solid State Chemistry, 1999. **144**(1): p. 220-223.
4. Hu, L., et al., *Symmetrical MnO2–carbon nanotube–textile nanostructures for wearable pseudocapacitors with high mass loading.* ACS nano, 2011. **5**(11): p. 8904-8913.
5. Toupin, M., T. Brousse, and D. Bélanger, *Charge storage mechanism of MnO2 electrode used in aqueous electrochemical capacitor.* Chemistry of Materials, 2004. **16**(16): p. 3184-3190.
6. Xiao, Y., et al., *Wearable pseudocapacitor based on porous MnO2 composite.* Journal of Alloys and Compounds, 2020. **813**: p. 152089.
7. Zhong, R., et al., *A flexible high-performance symmetric quasi-solid supercapacitor based on Ni-doped MnO2 nano-array@ carbon cloth.* Electrochimica Acta, 2020. **348**: p. 136209.
8. Liu, K.C. and M.A. Anderson, *Porous nickel oxide/nickel films for electrochemical capacitors.* Journal of the Electrochemical Society, 1996. **143**(1): p. 124.

9. Lu, Z., et al., *Stable ultrahigh specific capacitance of NiO nanorod arrays.* Nano Research, 2011. **4**(7): p. 658-665.

10. Lee, H.Y. and J. Goodenough, *Ideal supercapacitor behavior of amorphous V2O5· nH2O in potassium chloride (KCl) aqueous solution.* Journal of Solid State Chemistry, 1999. **148**(1): p. 81-84.

11. Gao, Y., et al., *Electrochemical capacitance of Co3O4 nanowire arrays supported on nickel foam.* Journal of Power Sources, 2010. **195**(6): p. 1757-1760.

12. Liu, S., et al., *Unlocking the potential of oxygen-deficient copper-doped Co3O4 nanocrystals confined in carbon as an advanced electrode for flexible solid-state supercapacitors.* ACS Energy Letters, 2021. **6**(9): p. 3011-3019.

13. Wang, L., et al., *Preparation of Fe 3 O 4 with high specific surface area and improved capacitance as a supercapacitor.* Nanoscale, 2013. **5**(9): p. 3793-3799.

14. Liu, X., et al., *Self-assembled porous NiCo2O4 hetero-structure array for electrochemical capacitor.* Journal of Power Sources, 2013. **239**: p. 157-163.

15. Wang, H., et al., *Ni (OH) 2 nanoplates grown on graphene as advanced electrochemical pseudocapacitor materials.* Journal of the American Chemical Society, 2010. **132**(21): p. 7472-7477.

16. Abushrenta, N., et al., *Hierarchical Co-based porous layered double hydroxide arrays derived via alkali etching for high-performance supercapacitors.* Scientific reports, 2015. **5**(1): p. 13082.

17. Shangguan, E., et al., *CoAl-layered double hydroxide nanosheets-coated spherical nickel hydroxide cathode materials with enhanced high-rate and*

*cycling performance for alkaline nickel-based secondary batteries.* Electrochimica Acta, 2020. **330**: p. 135198.

18. Patil, D.S., et al., *CoFe layered double hydroxide for enhanced electrochemical performance.* Journal of Electroanalytical Chemistry, 2020. **862**: p. 114012.
19. Ke, Q. and J. Wang, *Graphene-based materials for supercapacitor electrodes–A review.* Journal of Materiomics, 2016. **2**(1): p. 37-54.
20. Wang, J., et al., *Scalable synthesis of holey graphite nanosheets for supercapacitors with high volumetric capacitance.* Nanoscale Horizons, 2019. **4**(2): p. 526-530.
21. Fisher, R.A., M.R. Watt, and W.J. Ready, *Functionalized carbon nanotube supercapacitor electrodes: a review on pseudocapacitive materials.* ECS Journal of Solid State Science and Technology, 2013. **2**(10): p. M3170.
22. Yang, L., et al., *Hierarchical network architectures of carbon fiber paper supported cobalt oxide nanonet for high-capacity pseudocapacitors.* Nano letters, 2012. **12**(1): p. 321-325.
23. Guan, C., et al., *Iron oxide-decorated carbon for supercapacitor anodes with ultrahigh energy density and outstanding cycling stability.* ACS nano, 2015. **9**(5): p. 5198-5207.
24. Wilde, P., et al., *Strontium ruthenate perovskite as the active material for supercapacitors.* Journal of Electroanalytical Chemistry, 1999. **461**(1-2): p. 154-160.
25. Wohlfahrt-Mehrens, M., et al., *New materials for supercapacitors.* Journal of power sources, 2002. **105**(2): p. 182-188.
26. Klein, L., et al., *Anomalous spin scattering effects in the badly metallic itinerant ferromagnet SrRuO 3.* Physical review letters, 1996. **77**(13): p. 2774.

27. Hwang, D.K., et al., *Phase evolution of perovskite LaNiO 3 nanofibers for supercapacitor application and p-type gas sensing properties of LaOCl–NiO composite nanofibers.* Journal of Materials Chemistry, 2011. **21**(6): p. 1959-1965.

28. Mefford, J.T., et al., *Anion charge storage through oxygen intercalation in LaMnO3 perovskite pseudocapacitor electrodes.* Nature materials, 2014. **13**(7): p. 726-732.

29. Cao, Y., et al., *Symmetric/asymmetric supercapacitor based on the perovskite-type lanthanum cobaltate nanofibers with Sr-SUBSTITUTION.* Electrochimica Acta, 2015. **178**: p. 398-406.

30. Nan, H.-s., X.-y. Hu, and H.-w. Tian, *Recent advances in perovskite oxides for anion-intercalation supercapacitor: a review.* Materials Science in Semiconductor Processing, 2019. **94**: p. 35-50.

31. Fuertes, A.B. and M. Sevilla, *Superior Capacitive Performance of Hydrochar-Based Porous Carbons in Aqueous Electrolytes.* ChemSusChem, 2015. **8**(6): p. 1049-1057.

32. Bocquet, A., et al., *Electronic structure of SrFe 4+ O 3 and related Fe perovskite oxides.* Physical Review B, 1992. **45**(4): p. 1561.

33. Ghaffari, M., et al., *Band gap measurement of SrFeO 3− δ by ultraviolet photoelectron spectroscopy and photovoltage method.* CrystEngComm, 2012. **14**(21): p. 7487-7492.

34. Grenier, J., et al., *Electrochemical oxygen intercalation into oxide networks.* Journal of Solid State Chemistry, 1992. **96**(1): p. 20-30.

35. Ghaffari, M., et al., *Investigation of local structure effect and X-ray absorption characteristics (EXAFS) of Fe (Ti) K-edge on photocatalyst properties of SrTi*

*(1− x) FexO (3− δ).* Materials Chemistry and Physics, 2012. **136**(2-3): p. 347-357.

36. Liu, J., et al., *Conjugated copper–catecholate framework electrodes for efficient energy storage.* Angewandte Chemie International Edition, 2020. **59**(3): p. 1081-1086.

37. Yu, P., C. Li, and X. Guo, *Sodium storage and pseudocapacitive charge in textured Li4Ti5O12 thin films.* The Journal of Physical Chemistry C, 2014. **118**(20): p. 10616-10624.

38. Ardizzone, S., G. Fregonara, and S. Trasatti, *"Inner" and "outer" active surface of RuO2 electrodes.* Electrochimica Acta, 1990. **35**(1): p. 263-267.

39. Wang, J., et al., *Pseudocapacitive contributions to electrochemical energy storage in TiO2 (anatase) nanoparticles.* The Journal of Physical Chemistry C, 2007. **111**(40): p. 14925-14931.

40. Ji, S.-H., N.R. Chodankar, and D.-H. Kim, *Aqueous asymmetric supercapacitor based on RuO2-WO3 electrodes.* Electrochimica Acta, 2019. **325**: p. 134879.

41. Singha, S.S., et al., *Mn incorporated MoS2 nanoflowers: A high performance electrode material for symmetric supercapacitor.* Electrochimica Acta, 2020. **338**: p. 135815.

42. Fan, Y., et al., *PANI-Co3O4 with excellent specific capacitance as an electrode for supercapacitors.* Ceramics International, 2021. **47**(6): p. 8433-8440.

43. Dhandapani, P., et al., *A heterogeneous NiCo2O4@2D-carbyne nanohybrid – a new electrode material for robust and high energy density hybrid supercapacitors.* Sustainable Energy & Fuels, 2023. **7**(10): p. 2368-2377.

44. Azizi, S., et al., *High-capacity MnCo2O4/NiCo2O4 as electrode materials for electrochemical supercapacitors.* Journal of Physics and Chemistry of Solids, 2023. **174**: p. 111176.

45. Mishra, N.K., et al., *Synthesis, characterizations, and electrochemical performances of highly porous, anhydrous Co0. 5Ni0. 5C2O4 for pseudocapacitive energy storage applications.* ACS omega, 2022. **7**(2): p. 1975-1987.

46. Shen, L., et al., *Formation of nickel cobalt sulfide ball-in-ball hollow spheres with enhanced electrochemical pseudocapacitive properties.* Nature communications, 2015. **6**(1): p. 6694.

47. Kushwaha, V., et al., *Nanocrystalline β-NiS: a redox-mediated electrode in aqueous electrolyte for pseudocapacitor/supercapacitor applications.* Physical Chemistry Chemical Physics, 2023. **25**(1): p. 555-569.

48. Tang, Y., et al., *Morphology controlled synthesis of monodisperse cobalt hydroxide for supercapacitor with high performance and long cycle life.* Journal of Power Sources, 2014. **256**: p. 160-169.

49. Zheng, J., P. Cygan, and T. Jow, *Hydrous ruthenium oxide as an electrode material for electrochemical capacitors.* Journal of the Electrochemical Society, 1995. **142**(8): p. 2699.

50. Devaraj, S. and N. Munichandraiah, *Effect of crystallographic structure of MnO2 on its electrochemical capacitance properties.* The Journal of Physical Chemistry C, 2008. **112**(11): p. 4406-4417.

51. Wang, S.-Y., et al., *Investigation on capacitance mechanisms of Fe3O4 electrochemical capacitors.* Journal of the Electrochemical Society, 2005. **153**(1): p. A75.

52. Naiknaware, A., et al., *Studies on spray deposited Ni doped Mn3O4 electrodes for supercapacitor applications.* Journal of Alloys and Compounds, 2019. **774**: p. 787-794.

53. Chen, J., et al., *Pyrite FeS2 nanobelts as high-performance anode material for aqueous pseudocapacitor.* Electrochimica Acta, 2016. **222**: p. 172-176.

54. Quan, L., et al., *Construction of hierarchical nickel cobalt selenide complex hollow spheres for pseudocapacitors with enhanced performance.* Electrochimica Acta, 2018. **281**: p. 109-116.